Dynamics of fingering convection. Part 1 Small-scale fluxes and large-scale instabilities

A. TRAXLER[1]†, S. STELLMACH[1,2,3], P. GARAUD[1], T. RADKO[4] AND N. BRUMMELL[1]

[1]Applied Mathematics and Statistics, Baskin School of Engineering, University of California, Santa Cruz, CA 96064, USA

[2]Institut für Geophysik, Westfälische Wilhelms-Universität Münster, D-48149 Münster, Germany

[3]Institute of Geophysics and Planetary Physics, University of California, Santa Cruz, CA 96064, USA

[4]Department of Oceanography, Naval Postgraduate School, Monterey, CA 93943, USA

Double-diffusive instabilities are often invoked to explain enhanced transport in stably stratified fluids. The most-studied natural manifestation of this process, fingering convection, commonly occurs in the ocean's thermocline and typically increases diapycnal mixing by 2 orders of magnitude over molecular diffusion. Fingering convection is also often associated with structures on much larger scales, such as thermohaline intrusions, gravity waves and thermohaline staircases. In this paper, we present an exhaustive study of the phenomenon from small to large scales. We perform the first three-dimensional simulations of the process at realistic values of the heat and salt diffusivities and provide accurate estimates of the induced turbulent transport. Our results are consistent with oceanic field measurements of diapycnal mixing in fingering regions. We then develop a generalized mean-field theory to study the stability of fingering systems to large-scale perturbations using our calculated turbulent fluxes to parameterize small-scale transport. The theory recovers the intrusive instability, the collective instability and the γ-instability as limiting cases. We find that the fastest growing large-scale mode depends sensitively on the ratio of the background gradients of temperature and salinity (the density ratio). While only intrusive modes exist at high density ratios, the collective and γ instabilities dominate the system at the low density ratios where staircases are typically observed. We conclude by discussing our findings in the context of staircase-formation theory.

Key words: double-diffusive convection, geophysical and geological flows

1. Introduction

When the density of a fluid depends on (at least) two components, stably stratified systems can, under certain circumstances, undergo double-diffusive instabilities, leading to significant countergradient vertical buoyancy transport. Here, we focus on the case of the 'fingering' instability, which often occurs in fluids which are thermally stably stratified, but have an inhomogeneous composition. A well-known example is found in upper layers of the Earth's oceans where evaporation exceeds precipitation, leading to warm salty water overlaying colder fresh water (Stern 1960;

† Email address for correspondence: atraxler@soe.ucsc.edu

Schmitt *et al.* 2005). Since heat diffuses faster than salt, parcels of fluid displaced downward rapidly lose their excess heat while maintaining a larger salt concentration than the surrounding fluid. They become denser than the environment and continue to sink, forming structures called 'salt fingers'. Similar fingering instabilities can occur in any other thermally stably stratified solution, provided the concentration of the slower-diffusing solute increases with height (Stern 1960; Schmitt 1983).

The saturated state of this instability, fingering convection, takes the form of tightly packed vertically elongated plumes of sinking dense fluid and rising light fluid (Stern 1960; Kunze 2003) and significantly enhances the vertical transport of both heat and chemical composition. In the ocean, fingering convection increases diapycnal mixing within extended regions (Schmitt 1994; Kluikov & Karlin 1995; You 2002) of the thermocline by at least 2 orders of magnitude over molecular diffusion. It has been argued that the nutrient supply of the upper ocean (Dietze, Oschlies & Kähler 2004), the surface temperature and the surface fluxes of CO_2 and O_2 are all affected by this process (Glessmer, Oschlies & Yool 2008). Conditions favourable for fingering convection also exist in many other natural systems (Schmitt 1983). In the astrophysical context for example, a variety of situations lead to the development of unstable mean molecular weight gradients in otherwise stably stratified 'radiative' regions within stars and giant planets (Vauclair 2004; Charbonnel & Zahn 2007; Stancliffe *et al.* 2007). Since the long-term thermal evolution and chemical stratification of these objects are regulated by the transport bottleneck caused by radiative regions, the presence or absence of mixing by fingering convection can dramatically influence their observable properties (Garaud 2011; Traxler, Garaud & Stellmach 2011).

While fingering convection is by nature a small-scale phenomenon, it also has an intriguing propensity to generate dynamical structures on very large scales, such as internal gravity waves, thermohaline intrusions and thermohaline staircases. As first argued by Stern (1969) and Holyer (1981), a homogeneous field of fingers can become unstable to the so-called 'collective instability', leading to the spontaneous generation of internal gravity waves in regions of active salt fingering. This instability was later confirmed in direct numerical simulations (DNSs) by Stern, Radko & Simeonov (2001).

Thermohaline intrusions are different kinds of large-scale structures which are nevertheless also often associated with the fingering convection. They take the form of laterally interleaving layers with distinct temperature and salinity signatures and can spontaneously form in fluids which are stratified *both* vertically and horizontally. They are commonly observed in the ocean (Ruddick & Richards 2003) and have been reproduced in laboratory experiments (Ruddick & Turner 1979; Ruddick, Phillips & Turner 1999) and numerically (Simeonov & Stern 2007). For a detailed discussion of intrusion theory, see Toole & Georgi (1981), McDougall (1985*a*, *b*) or Ruddick & Kerr (2003) for a recent review.

Finally, one of the most dramatic signatures of active fingering convection in the ocean is the formation of mixed layers separated by salt finger interfaces, known as thermohaline staircases. Persistent staircases have been documented in the Tyrrhenian Sea, below the Mediterranean outflow, and in the western tropical North Atlantic (Schmitt 1994). Layer formation is also observed in laboratory experiments (Stern & Turner 1969; Krishnamurti 2003). Layering enhances vertical mixing by up to an order of magnitude (Schmitt *et al.* 2005; Veronis 2007) relative to globally similarly stratified regions characterised by a smoother stratification. Forty years after the discovery of this phenomenon in oceanographic field measurements (Tait & Howe 1968, 1971), a generally accepted explanation is still lacking. Radko (2003) argued

through theoretical and numerical analyses that the observed layering is likely to be caused by the so-called γ-instability – an instability driven by variations in the ratio of the turbulent heat and salt fluxes.

The conventional approach to analyse the spontaneous generation of structures from fingering convection uses the assumed separation of scale between the finger scale and the emerging structure scale to construct a mean-field theory, in which the effect of the small-scale fingering is modelled through turbulent fluxes. The resulting mean-field equations describe the evolution of the large-scale fields only and can be analysed for linear stability. Globally speaking, the modulation of the background stratification by large-scale temperature and salinity perturbations induces a modulation of the turbulent fluxes. When the divergence or convergence of these modified fluxes act to enhance the original perturbation, large-scale modes of instability are excited. Different variants of mean-field models have been individually successful in representing the gross properties of each of the aforementioned large-scale phenomena (intrusions, collective instability and γ-instability).

In this paper, we show that these various modes of instability can actually be described by a single unifying mean-field formalism and are all recovered as limiting cases of our theory – each one corresponding to a different feedback mechanism between the large-scale perturbation and the induced turbulent fluxes. In §2 we present our unified mean-field model and its relationship with previous work. In §3, we then perform a series of three-dimensional simulations for parameter values typical of salty water in the ocean, designed to measure the turbulent transport of heat and salt as parametric functions of the background stratification.

Using the small-scale flux laws derived, we then calculate and discuss in §4 the expected growth rates of the various large-scale modes of instability as functions of the overall stratification of the region. Our results indicate that the relative importance of these various modes is highly sensitive to the density ratio (the ratio of the vertical temperature and salinity gradients normalised by their expansion/contraction coefficients). For low density ratio the dynamics of the system is primarily controlled by the collective and γ instabilities. For intermediate density ratios, the γ-instability is suppressed and the dynamics is dominated by gravity waves, with intrusive modes gaining importance. For larger values of the density ratio, only intrusive modes are unstable.

Finally, we discuss our findings in §5, focusing on the implication of the measured turbulent fluxes for oceanic mixing in §5.1 and on the role of the large-scale instabilities studied in the formation of thermohaline staircases in §5.2. Further detail on the last point is given in Stellmach *et al.* (2011, hereafter referred to as Part 2) where a large-domain three-dimensional simulation of fingering convection is followed through spontaneous layer formation and analysed with the unified theory developed below.

2. Generalised mean-field theory of fingering convection

2.1. *The governing equations for homogeneous fingering convection*

Fingering convection, when observed in natural systems, typically occurs far from physical boundaries. For this reason, we adopt an approach which minimises boundary effects by considering triply periodic temperature, salinity and velocity perturbations driven by a steady and uniform fingering-unstable background stratification. This set-up has been advocated by others before for studying fingering convection (Stern *et al.* 2001; Radko 2003) and is ideally suited to numerical simulations using spectral methods (see §3 and Part 2). It is important to note that it does not suffer from

the well-known pathology of thermal convection in a triply periodic system – the so-called homogeneous Rayleigh–Bénard problem (Borue & Orszag 1996; Calzavarini *et al.* 2006), where the fastest growing modes (FGWs) span the entire domain and depend sensitively on the aspect ratio of the box. Instead, the typical length scale of convective motions in the fingering regime is set by the diffusive length scales and is independent of the box size, provided the box is large enough (see the Appendix).

We consider a Cartesian coordinate system (x, y, z) with z increasing upward in the vertical direction. In all that follows, we use the Boussinesq approximation. We assume that the background temperature and salinity profiles, $T_0(x, z)$ and $S_0(x, z)$, are bilinear functions of x and z, $T_0(x, z) = T_{0x}x + T_{0z}z$ and $S_0(x, z) = S_{0x}x + S_{0z}z$. Without loss of generality, the background fields are assumed to be two dimensional by aligning the horizontal gradients with the x-axis. We assume (as in Walsh & Ruddick (1995)) that the overall horizontal density gradient is zero, in which case $\alpha T_{0x} - \beta S_{0x} = 0$, where α and β are the coefficients of thermal expansion and compositional contraction, respectively. The slope of the background temperature gradient in this coordinate system is $\phi = T_{0x}/T_{0z}$.

We perform a standard non-dimensionalisation procedure for studying local fingering convection. We use the expected finger scale (see Stern 1960) as the length scale, $[l] = d = (\kappa_T \nu / g \alpha T_{0z})^{1/4}$, where g is gravity, ν is viscosity and κ_T is thermal diffusivity. We then define the corresponding thermal diffusion time scale, $[t] = d^2/\kappa_T$, the velocity scale, $[u] = \kappa_T/d$, pressure scale, $[p] = \nu\kappa_T/d^2$ and the temperature and salinity scales, $[T] = T_{0z}d$ and $[S] = (\alpha/\beta)T_{0z}d$. Non-dimensional parameters of interest are the Prandtl number, $Pr = \nu/\kappa_T$, the background density ratio, $R_0 = \alpha T_{0z}/\beta S_{0z}$, and the diffusivity ratio, $\tau = \kappa_S/\kappa_T$.

The non-dimensional equations for the evolution of the velocity field $\boldsymbol{u} = (u, v, w)$ and the temperature and salinity perturbations $T(x, y, z, t)$ and $S(x, y, z, t)$ are then

$$\frac{1}{Pr}\left(\frac{\partial \boldsymbol{u}}{\partial t} + \boldsymbol{u}\cdot\nabla\boldsymbol{u}\right) = -\nabla p + (T - S)\hat{\boldsymbol{k}} + \nabla^2\boldsymbol{u}, \tag{2.1a}$$

$$\nabla\cdot\boldsymbol{u} = 0, \tag{2.1b}$$

$$\frac{\partial T}{\partial t} + \phi u + w + \boldsymbol{u}\cdot\nabla T = \nabla^2 T, \tag{2.1c}$$

$$\frac{\partial S}{\partial t} + \phi u + \frac{1}{R_0}w + \boldsymbol{u}\cdot\nabla S = \tau\nabla^2 S, \tag{2.1d}$$

where p is the non-dimensional pressure perturbation from hydrostatic equilibrium and $\hat{\boldsymbol{k}}$ is the unit vector in the z-direction.

2.2. *Generalised mean-field theory*

As discussed in §1, fingering convection is often associated with the emergence of dynamical structures on scales much larger than individual fingers. We begin by deriving a generalised set of mean-field equations and then study their linear stability to various large-scale modes.

2.2.1. *Mean-field equations*

As in Radko (2003), we are interested in the large-scale behaviour of the system of equations (2.1*a*)–(2.1*d*) when averaged over spatial/temporal scales of many fingers. We introduce the notation $\overline{\cdots}$, where the overbar denotes an averaging process which we assume may commute with the spatial and temporal derivatives. Let $\boldsymbol{u} = \bar{\boldsymbol{u}} + \boldsymbol{u}'$ and similarly for T and S, in which case $\overline{\boldsymbol{u}'} = \overline{T'} = \overline{S'} = 0$. The averaged governing

equations now become

$$\frac{1}{Pr}\left(\frac{\partial \overline{\boldsymbol{u}}}{\partial t} + \overline{\boldsymbol{u}} \cdot \nabla \overline{\boldsymbol{u}}\right) = -\nabla \overline{p} + (\overline{T} - \overline{S})\hat{\boldsymbol{k}} + \nabla^2 \overline{\boldsymbol{u}} - \frac{1}{Pr}\nabla \cdot \boldsymbol{R}, \qquad (2.2a)$$

$$\frac{\partial \overline{T}}{\partial t} + \phi \overline{u} + \overline{w} + \overline{\boldsymbol{u}} \cdot \nabla \overline{T} = \nabla^2 \overline{T} - \nabla \cdot \boldsymbol{F}_T, \qquad (2.2b)$$

$$\frac{\partial \overline{S}}{\partial t} + \phi \overline{u} + \frac{1}{R_0}\overline{w} + \overline{\boldsymbol{u}} \cdot \nabla \overline{S} = \tau \nabla^2 \overline{S} - \nabla \cdot \boldsymbol{F}_S, \qquad (2.2c)$$

where $R_{ij} = \overline{u_i' u_j'}$, and the turbulent fluxes are $\boldsymbol{F}_T = \overline{\boldsymbol{u}'T'}$ and $\boldsymbol{F}_S = \overline{\boldsymbol{u}'S'}$.

In what follows we now drop the overbar and only refer to the evolution of the large-scale fields $\boldsymbol{u}$, T and S. As in previous analyses, we assume that the Reynolds stress term is small enough to neglect (a fact that is easily verified *a posteriori*) and additionally assume that only the vertical components of the heat and salt fluxes are large enough to be significant (so that $\boldsymbol{F}_T \approx F_T \hat{\boldsymbol{k}}$ and $\boldsymbol{F}_S \approx F_S \hat{\boldsymbol{k}}$). However, we retain the diffusion terms in all three equations. The turbulent fluxes are measured by the non-dimensional Nusselt number Nu and the turbulent flux ratio γ, defined as

$$Nu = \frac{F_T - (1 + \partial T/\partial z)}{-(1 + \partial T/\partial z)}, \qquad (2.3)$$

$$\gamma = \frac{F_T}{F_S}. \qquad (2.4)$$

Note that these definitions of Nu and γ differ somewhat from those of Radko (2003), who includes the molecular diffusion terms in his definition of F_T and F_S. Our formalism has greater generality, since it allows for horizontal diffusive fluxes. The difference becomes important at low Nusselt number.

We now make the key assumption that at any given time both Nu and γ depend only on the local value of the density ratio R_ρ,

$$R_\rho = \frac{\alpha T_{0z}(1 + \partial T/\partial z)}{\beta S_{0z}\left[1 + \left(\frac{\alpha T_{0z}}{\beta S_{0z}}\right)\partial S/\partial z\right]} = R_0 \frac{1 + \partial T/\partial z}{1 + R_0 \partial S/\partial z}. \qquad (2.5)$$

Note that R_ρ may vary in time and space, while the background R_0 is fixed. The functions $Nu(R_\rho)$ and $\gamma(R_\rho)$ can be determined experimentally using numerical simulations (see §3).

The system of equations describing the evolution of the large-scale quantities $\boldsymbol{u}$, T and S is now

$$\frac{1}{Pr}\left(\frac{\partial \boldsymbol{u}}{\partial t} + \boldsymbol{u} \cdot \nabla \boldsymbol{u}\right) = -\nabla p + (T - S)\hat{\boldsymbol{k}} + \nabla^2 \boldsymbol{u}, \qquad (2.6a)$$

$$\frac{\partial T}{\partial t} + \phi u + w + \boldsymbol{u} \cdot \nabla T = \nabla^2 T - \frac{\partial F_T}{\partial z}, \qquad (2.6b)$$

$$\frac{\partial S}{\partial t} + \phi u + \frac{1}{R_0}w + \boldsymbol{u} \cdot \nabla S = \tau \nabla^2 S - \frac{\partial F_S}{\partial z}, \qquad (2.6c)$$

where the flux derivative terms on the right-hand side will use (2.3) and (2.4) to express F_T and F_S in terms of Nu and γ.

2.2.2. *Linearised mean-field theory*

The mean-field equations derived above exhibit steady solutions describing a state of homogeneous fingering convection, with zero mean velocity, zero deviation from the background temperature and salinity fields and constant (non-dimensional) heat and salinity fluxes $F_{T0} = (1 - Nu_0(R_0))$ and $F_{S0} = \gamma(R_0)/F_{T0}$. The stability of this homogenous turbulent state can be investigated by adding a small perturbation to the mean quantities and linearising the mean-field equations. Large-scale temperature and salinity perturbations induce large-scale variations in the density ratio, so that $R_\rho = R_0 + R'_\rho$. This, in turn, modulates the turbulent fluxes in a way which may further enhance the initial perturbations or quench them. Various modes of instability are related to different feedback mechanisms between the fields and turbulent fluxes, through the parametric functions $Nu(R_\rho)$ and $\gamma(R_\rho)$.

Assuming that perturbations away from the linear background gradients are small, we first have, expanding (2.5) to linear order,

$$R_\rho = R_0 \left(1 + \frac{\partial T}{\partial z} - R_0 \frac{\partial S}{\partial z} \right) = R_0 + R'_\rho, \tag{2.7}$$

which uniquely defines R'_ρ, and then

$$Nu(R_\rho) \approx Nu(R_0) + \left. \frac{\mathrm{d}Nu}{\mathrm{d}R_\rho} \right|_{R_0} R'_\rho, \tag{2.8}$$

and similarly for γ. Rearranging (2.3) and (2.4) yields $F_T = (1 - Nu)(1 + \partial T/\partial z)$ and $F_S = F_T/\gamma$. It then follows that

$$-\frac{\partial F_T}{\partial z} = A_2 \left(\frac{\partial^2 T}{\partial z^2} - R_0 \frac{\partial^2 S}{\partial z^2} \right) + (Nu_0 - 1) \frac{\partial^2 T}{\partial z^2}, \tag{2.9}$$

$$-\frac{\partial F_S}{\partial z} = A_1 \left(\frac{\partial^2 T}{\partial z^2} - R_0 \frac{\partial^2 S}{\partial z^2} \right)(Nu_0 - 1) - \frac{1}{\gamma_0} \frac{\partial F_T}{\partial z}, \tag{2.10}$$

where we have abbreviated $Nu(R_0) = Nu_0$, $\gamma(R_0) = \gamma_0$ and defined

$$A_1 = R_0 \frac{\partial \gamma^{-1}}{\partial R_\rho}, \tag{2.11}$$

$$A_2 = R_0 \frac{\partial Nu}{\partial R_\rho}. \tag{2.12}$$

Note that our A_1 and A_2 are not strictly equal to those defined by Radko (2003), but reduce to the same quantities in the limit where turbulent fluxes are much larger than diffusive fluxes.

A standard linear stability analysis of (2.6), using normal modes of the form $\{u, T, S\} = \{\hat{u}, \hat{T}, \hat{S}\} \exp(\lambda t + ilx + imy + ikz)$, yields a cubic equation for the growth rate, $\lambda^3 + a_2 \lambda^2 + a_1 \lambda + a_0 = 0$, with

$$a_2 = |\mathbf{k}|^2 (1 + Pr + \tau) + k^2 \left[(1 - A_1 R_0)(Nu_0 - 1) + A_2 \left(1 - \frac{R_0}{\gamma_0} \right) \right], \tag{2.13a}$$

$$a_1 = |\mathbf{k}|^4 (\tau Pr + \tau + Pr) + k^2 |\mathbf{k}|^2 \left[(\tau + Pr)(A_2 + Nu_0 - 1) - A_2(1 + Pr) \frac{R_0}{\gamma_0} \right.$$
$$\left. - A_1 R_0 (1 + Pr)(Nu_0 - 1) \right] - k^4 A_1 R_0 (Nu_0 - 1)^2 + Pr \frac{l^2}{|\mathbf{k}|^2} \frac{l^2 + m^2}{l^2} \left(1 - \frac{1}{R_0} \right), \tag{2.13b}$$

$$a_0 = |\boldsymbol{k}|^6 \tau \, Pr + k^2 |\boldsymbol{k}|^4 \, Pr \left[(\tau - A_1 R_0)(Nu_0 - 1) + A_2 \left(\tau - \frac{R_0}{\gamma_0} \right) \right]$$

$$- k^4 |\boldsymbol{k}|^2 \, Pr \, R_0 A_1 (Nu_0 - 1)^2 + Pr \frac{l}{|\boldsymbol{k}|^2} \left\{ |\boldsymbol{k}|^2 \left[l \frac{l^2 + m^2}{l^2} \left(\tau - \frac{1}{R_0} \right) - k\phi(\tau - 1) \right] \right.$$

$$+ k^2 A_1 (1 - R_0)(Nu_0 - 1) \left(l \frac{l^2 + m^2}{l^2} - k\phi \right) - k^2 [A_2 (1 - R_0)$$

$$\left. + Nu_0 - 1] \left[l \frac{l^2 + m^2}{l^2} \left(\frac{1}{R_0} - \frac{1}{\gamma_0} \right) - k\phi \left(1 - \frac{1}{\gamma_0} \right) \right] \right\}, \tag{2.13c}$$

where $|\boldsymbol{k}|^2 = k^2 + l^2 + m^2$.

2.2.3. *Relationship with previous theories*

Presented above is a unified formulation of several mean-field theories, including the effects of all diffusion terms and the contribution of variable turbulent flux ratio γ as well as allowing for the presence of lateral background gradients in temperature and salinity. Several limiting cases have been discussed previously in the literature (unless otherwise noted these are two-dimensional theories, so $m = 0$).

The fingering instability. Although technically not a mean-field instability, it is reassuring to note that the fingering instability itself (e.g. Baines & Gill 1969) is recovered when turbulent fluxes and lateral gradients are ignored ($A_1 = A_2 = Nu_0 - 1 = \phi = 0$). In that case the cubic defined by (2.13) becomes the well-known cubic equation for the growth rates of the fingering modes with

$$a_2 = |\boldsymbol{k}|^2 (1 + Pr + \tau), \tag{2.14a}$$

$$a_1 = |\boldsymbol{k}|^4 (\tau \, Pr + \tau + Pr) + Pr \frac{l^2}{|\boldsymbol{k}|^2} \left(1 - \frac{1}{R_0} \right), \tag{2.14b}$$

$$a_0 = |\boldsymbol{k}|^6 \tau \, Pr + Pr \, l^2 \left(\tau - \frac{1}{R_0} \right). \tag{2.14c}$$

The collective instability, as derived by Stern et al. (2001), is recovered from (2.13) by omitting lateral gradients ($\phi = 0$), neglecting possible variation in γ (so $A_1 = 0$) and discarding the diffusion terms for temperature and salinity but retaining viscosity in (2.2).

$$a_2 = Pr |\boldsymbol{k}|^2 + k^2 \left[A_2 \left(1 - \frac{R_0}{\gamma_0} \right) + Nu_0 - 1 \right], \tag{2.15a}$$

$$a_1 = Pr k^2 |\boldsymbol{k}|^2 \left[A_2 \left(1 - \frac{R_0}{\gamma_0} \right) + Nu_0 - 1 \right] + Pr \frac{l^2}{|\boldsymbol{k}|^2} \left(1 - \frac{1}{R_0} \right), \tag{2.15b}$$

$$a_0 = Pr \frac{k^2 l^2}{|\boldsymbol{k}|^2} [A_2 (1 - R_0) + Nu_0 - 1] \left(\frac{1}{\gamma_0} - \frac{1}{R_0} \right). \tag{2.15c}$$

Stern (1969) argued that modes are excited when the Stern number, written in our notation as

$$A = \frac{(Nu_0 - 1) \left(\frac{1}{\gamma_0} - 1 \right)}{Pr \left(1 - \frac{1}{R_0} \right)}, \tag{2.16}$$

exceeds a value of the order of 1. The unstable modes essentially represent overstable gravity waves.

An elegant physical interpretation (Stern *et al.* 2001) of the collective instability is obtained by analogy with the laminar linear double-diffusive instability in the 'diffusive regime', where the slowly diffusing field is stably stratified, while the rapidly diffusing field is unstably stratified. In this case, growing oscillatory modes akin to internal gravity waves are excited instead of fingers. Since fingering convection induces a mean salt flux larger than the heat flux, the roles of the two fields are reversed, and the faster diffusing field is now the salinity field. From a turbulent point of view, the 'diffusive regime' is recovered.

The theory of intrusions of Walsh & Ruddick (1995) is recovered by discarding the diffusion terms in (2.2) and setting γ constant ($A_1 = 0$) as well as neglecting Reynolds stresses in their formulation,

$$a_2 = k^2 \left[A_2 \left(1 - \frac{R_0}{\gamma_0} \right) + (Nu_0 - 1)(1 - A_1 R_0) \right], \tag{2.17a}$$

$$a_1 = -k^4 R_0 (Nu_0 - 1)^2 A_1 + Pr \frac{l^2}{|\boldsymbol{k}|^2} \left(1 - \frac{1}{R_0} \right), \tag{2.17b}$$

$$a_0 = Pr \frac{lk^2}{|\boldsymbol{k}|^2} \left\{ [A_2(1 - R_0) + Nu_0 - 1] \left[k\phi \left(1 - \frac{1}{\gamma_0} \right) + l \left(\frac{1}{\gamma_0} - \frac{1}{R_0} \right) \right] \right.$$
$$\left. + A_1(1 - R_0)(Nu_0 - 1)(l - k\phi) \right\}. \tag{2.17c}$$

The mechanism underlying intrusive instabilities can be illustrated by imagining an alternating horizontal shear flow superimposed on the background stratification (see, e.g., Ruddick & Kerr 2003). Alternating vertical variations in R_ρ result, which in turn strengthens or weakens the fingering action, and the resulting flux convergences and divergences reinforce the intrusive motion. Depending on the orientation of the perturbation, both direct and oscillatory modes are possible (Walsh & Ruddick 1995).

The γ-instability, as derived in Radko (2003), is recovered by considering horizontally invariant perturbations ($l = m = 0$, $|\boldsymbol{k}|^2 = k^2$) with zero velocity field. From the remaining temperature and salinity equations, we obtain a quadratic expression for the growth rate (To see why our formalism yields a cubic while Radko's yields a quadratic, it should be noted that (2.13) can be factored with $l = m = 0$ as $(\lambda + k^2 Pr)(\lambda^2 + b_1\lambda + b_0)$. The first root describes the viscous decay of any initial velocity perturbation.),

$$a_2 = 1, \tag{2.18a}$$

$$a_1 = k^2 \left[1 + \tau + (1 - A_1 R_0)(Nu_0 - 1) + A_2 \left(1 - \frac{R_0}{\gamma_0} \right) \right], \tag{2.18b}$$

$$a_0 = k^4 \left[(\tau - A_1 R_0)(Nu_0 - 1) - A_1 R_0 (Nu_0 - 1)^2 + A_2 \left(\tau - \frac{R_0}{\gamma_0} \right) \right]. \tag{2.18c}$$

Differences between these coefficients and those given in Radko (2003) arise from our alternate definition of γ, but can be shown to be reduced to each other in the limit of large Nusselt number. However note that for γ-modes, which do not have any horizontal variation, the use of the total fluxes $F_T^{tot} = F_T - (1 + \partial T/\partial z)$

and $F_S^{tot} = F_S - \tau(1/R_0 + \partial S/\partial z)$ (originally advocated by Radko) recovers his much simpler quadratic, with

$$a_2 = 1, \tag{2.19a}$$

$$a_1 = k^2 \left[(1 - A_1^{tot} R_0) Nu_0 + A_2 \left(1 - \frac{R_0}{\gamma_0^{tot}} \right) \right], \tag{2.19b}$$

$$a_0 = -k^4 A_1^{tot} R_0 Nu_0^2, \tag{2.19c}$$

where $\gamma_0^{tot} = F_T^{tot}/F_S^{tot}$ and $A_1^{tot} = R_0 \mathrm{d}(1/\gamma^{tot})/\mathrm{dR}_\rho$. As shown by Radko, a sufficient condition for the existence of a positive real root is that $A_1^{tot} > 0$, or in other words that γ^{tot} should be a decreasing function of R_ρ. The physical interpretation of this so-called 'γ-instability' is fairly subtle and is described in detail in the original paper (Radko 2003).

3. Turbulent flux laws

To proceed forward and estimate growth time scales for the various mean-field modes of instability excited by fingering convection, we need to determine the non-dimensional turbulent fluxes Nu and γ as functions of the density ratio. Naturally, these depend on the diffusivity ratios Pr and τ relevant to the system studied. Here, we choose to focus on the case of salty water ($Pr = 7$ and $\tau = 0.01$), as it is directly applicable to the oceanographic context. We solve equations (2.1a)–(2.1d) numerically for a range of values of R_ρ (here we use R_ρ and R_0 interchangeably). The Appendix summarises the numerical algorithm, describes the experimental protocol for determining heat and salt fluxes and discusses the problem of selection of the domain size to be used for these experiments. What follows are the results of a body of simulations at different density ratios R_ρ.

3.1. *Typical results*

Figure 1 shows a visualisation of the salinity field obtained in the saturated state of a fingering system with $R_\rho = 1.2$, $R_\rho = 2$ and $R_\rho = 10$. On account of the small diffusivity of salt compared with all other fields, a broad range of spatial scales exists, and a high numerical resolution is *a priori* required to resolve all arising structures and correctly model the system. We find that, as expected, the salinity field has a complicated structure for small R_ρ, but successively becomes more organised with increasing density ratio. Regular, vertically elongated filamentary structures dominate for $R_\rho \geqslant 10$. In order to ensure that the smallest scales of the salinity field are fully resolved, we had to use the highest resolution available (a grid of $768 \times 768 \times 1536$) at $R_\rho = 1.2$, although half of that resolution is sufficient for $R_\rho \geqslant 2$. Furthermore, it turns out that a rough estimate of the flux laws can in fact be made with a much coarser resolution – for example, a 96^3 grid at $R_\rho = 4$ yields fluxes within 20 % of their corresponding fully resolved values (see table 1). This rather surprising result shows that the diffusion of salt does not play an important role in controlling the mixing in the heat–salt system, for very turbulent flows (low R_ρ). Moreover, it suggests that the processes operating on the salt dissipation scale play a passive role in the dynamics of salt fingers and the rate of salt dissipation is controlled by much larger heat dissipation scales.

3.2. *Turbulent flux laws for the heat–salt system*

The control parameters used in each simulation, along with some key results, are summarised in table 1. Plots displaying the most important findings are shown in
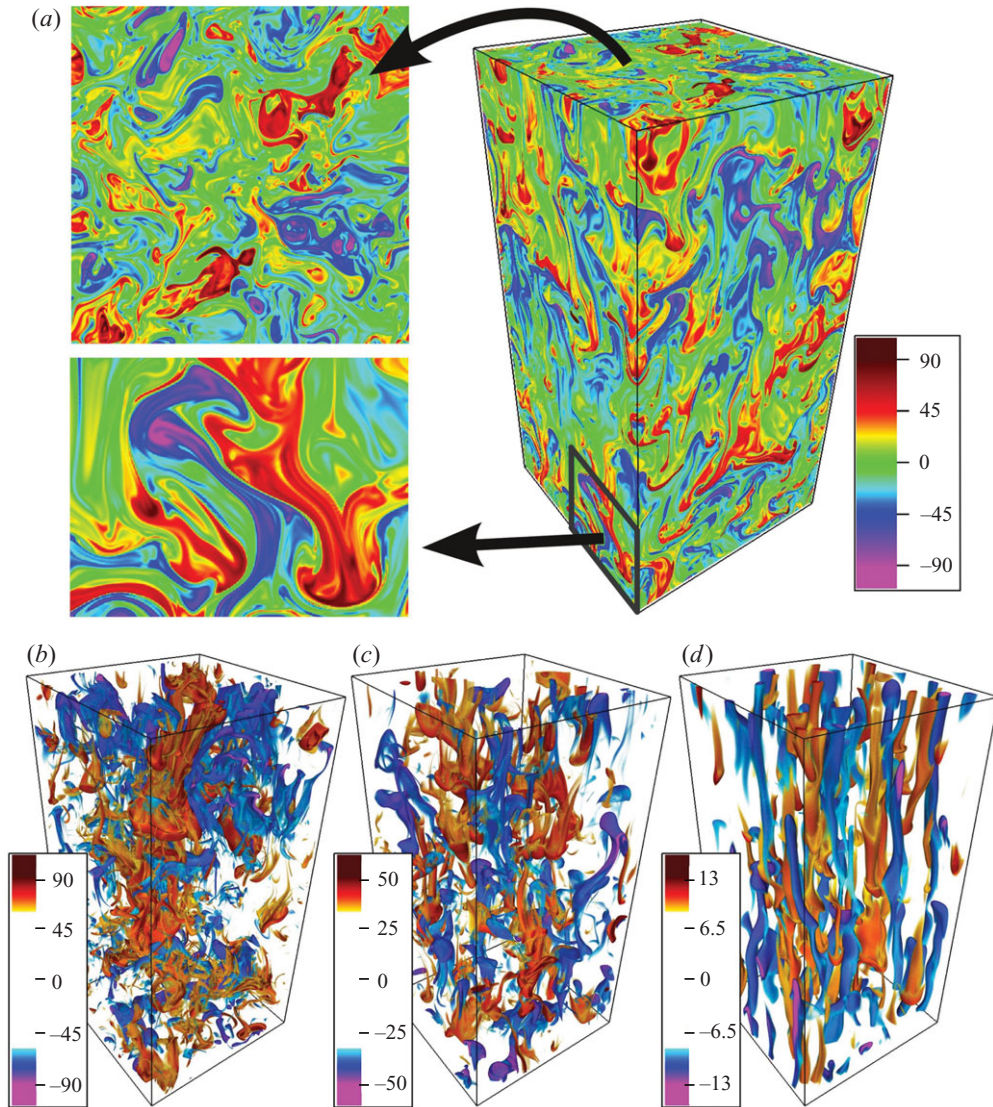
FIGURE 1. Snapshots of the salinity field S in simulations of fingering convection in the heat–salt system ($Pr = 7$, $\tau = 0.01$). (a) Salinity field at $R_\rho = 1.2$, plotted on the three planes $x = 0$, $y = 0$ and $z = L_z$. (b–d) Volume rendering of the salinity field for $R_\rho = 1.2$, $R_\rho = 2$ and $R_\rho = 10$ (from left to right). In all cases, the simulation domain contains $5 \times 5 \times 10$ FGW (see main text). Note how the typical amplitude of the salinity perturbation in a finger is of the order of $1/R_\rho \tau$, or, in dimensional terms, dS_{oz}/τ.

figure 2, which also contains results from an accompanying set of two-dimensional simulations.

As expected, we find that the turbulent fluxes $|F_S|$ and $|F_T|$ decrease rapidly with increasing density ratio and tend to be considerably larger in the three-dimensional case than in the two-dimensional case. The ratio of three-dimensional to two-dimensional fluxes is not constant, but tends to grow with increasing R_ρ. Because of their obvious oceanic relevance, table 1 also lists values for the 'eddy' diffusivities
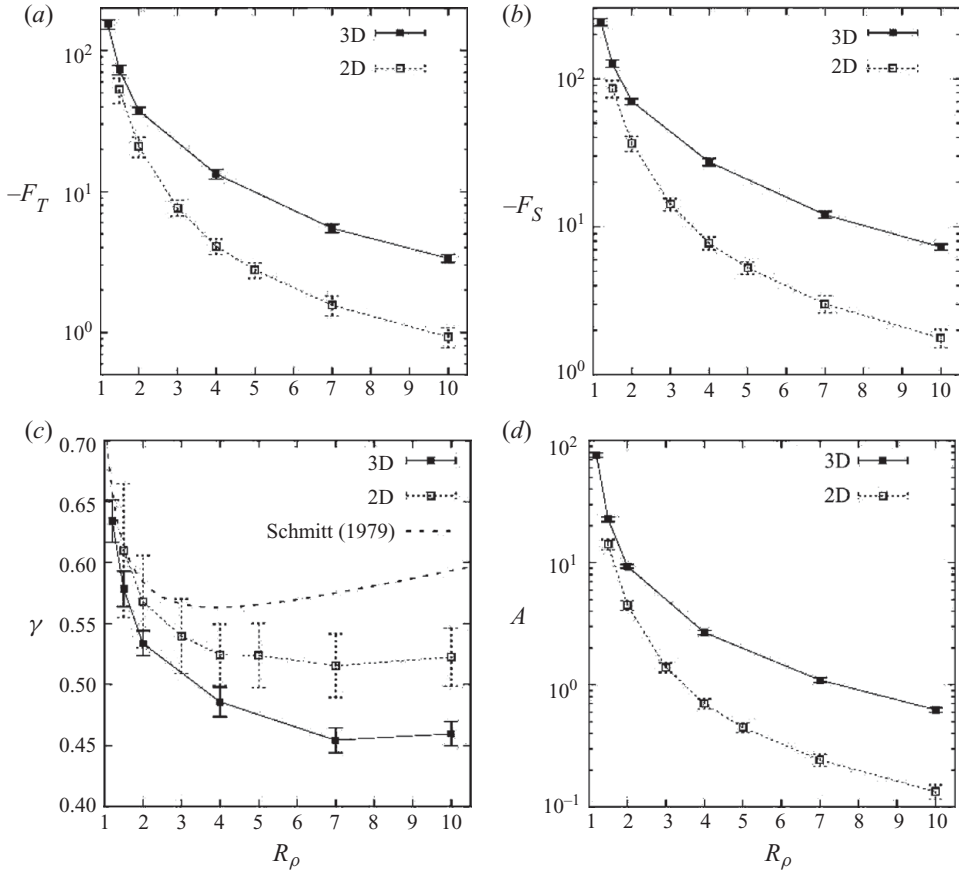
FIGURE 2. Parametric dependence of the non-dimensional fluxes F_T and F_S as well as their ratio γ and of the Stern number A as a function of R_ρ. Results from both three- and two-dimensional simulations are shown. Panel (c) also contains a theoretical prediction of $\gamma(R_\rho)$ based on the fastest growing linear modes (Schmitt 1979).

$K_T = \kappa_T |F_T|$ and $K_S = \kappa_T R_\rho |F_S|$ of heat and salt. At $R_\rho = 1.2$, we find $K_T \approx 21 \times 10^{-6} \, \mathrm{m}^2$ s^{-1} and $K_S \approx 41 \times 10^{-6} \, \mathrm{m}^2 \, \mathrm{s}^{-1}$. Both quantities quickly decrease with increasing R_ρ.

The turbulent flux ratio γ tends to be larger in the two-dimensional case than in the three-dimensional case. It initially decreases quickly with growing R_ρ, attains a minimum around $R_\rho \approx 7$ ($\gamma \approx 0.45$ in the three-dimensional case) and then slowly increases again. A widely used theoretical prediction based on linearly fastest growing modes, originally proposed by Schmitt (1979), tends to overestimate γ considerably and also predicts the minimum to occur at a smaller ($R_\rho = 4$) value of R_ρ. The total flux ratio γ^{tot} (see §2.2), which plays a prominent role in the γ-instability theory, is shown in figure 3. Its value deviates significantly from the turbulent flux ratio γ at higher values of R_ρ, where the Nusselt number is lower. As a result, the position of the minimum of the curve occurs for lower R_ρ, thus restricting the range for which the γ-instability is expected to $R_\rho \leqslant 4$. Furthermore, since the growth rate of the instability is proportional to $\mathrm{d}(1/\gamma^{tot})/\mathrm{dR}_\rho$, we find that γ-modes should only be significant for $R_\rho \leqslant 2$.

	$R_\rho = 1.2$	$R_\rho = 1.5$	$R_\rho = 2.0$	$R_\rho = 4$	$R_\rho = 7$	$R_\rho = 10$
Resolution	$768^2 \times 1536$	$768^2 \times 1536$	$384^2 \times 768$	$384^2 \times 768$	$384^2 \times 768$	$384^2 \times 768$
$\Delta t_{average}$	39.1	57.8	121.2	223.8	422.7	390.1
$|F_T|$	153.5 ± 11.7	73.2 ± 5.7	37.6 ± 2.2	13.3 ± 1.0	5.48 ± 0.38	3.35 ± 0.21
$|F_S|$	241.8 ± 13.1	126.4 ± 7.5	70.3 ± 3.1	27.4 ± 1.5	12.1 ± 0.65	7.29 ± 0.34
γ	0.63 ± 0.02	0.58 ± 0.01	0.53 ± 0.01	0.49 ± 0.01	0.45 ± 0.01	0.46 ± 0.01
$\sqrt{\langle u^2 \rangle}$	14.1 ± 0.4	9.4 ± 0.3	6.5 ± 0.15	3.7 ± 0.1	2.37 ± 0.06	1.82 ± 0.04
K_T $[10^{-6}\,\mathrm{m^2\,s^{-1}}]$	21 ± 2	10 ± 1	5.3 ± 0.3	1.9 ± 0.1	0.77 ± 0.05	0.47 ± 0.03
K_S $[10^{-6}\,\mathrm{m^2\,s^{-1}}]$	41 ± 2	27 ± 2	20 ± 1	15 ± 1	11 ± 1	10 ± 0.5
A	76 ± 3	23 ± 1	9.4 ± 0.3	2.7 ± 0.1	1.1 ± 0.05	0.63 ± 0.03

TABLE 1. Summary of simulations of homogeneous fingering convection for the heat–salt system ($\tau = 0.01$, $Pr = 7$) in a computational domain containing $5 \times 5 \times 10$ fastest growing finger wavelengths (FGW, see Schmitt 1979). $\Delta t_{average}$ denotes the length of the time interval over which the data have been averaged, $K_T = \kappa_T |F_T|$ and $K_S = \kappa_T R_\rho |F_S|$ are the 'eddy' diffusivities for heat and salt, taking $\kappa_T = 1.4 \times 10^{-7}\mathrm{m^2\,s^{-1}}$, and A is the Stern number defined in (2.16). Note that these eddy diffusivities apply to regions of homogeneous fingering convection and may be strongly increased in the presence of thermohaline staircases as mentioned above.
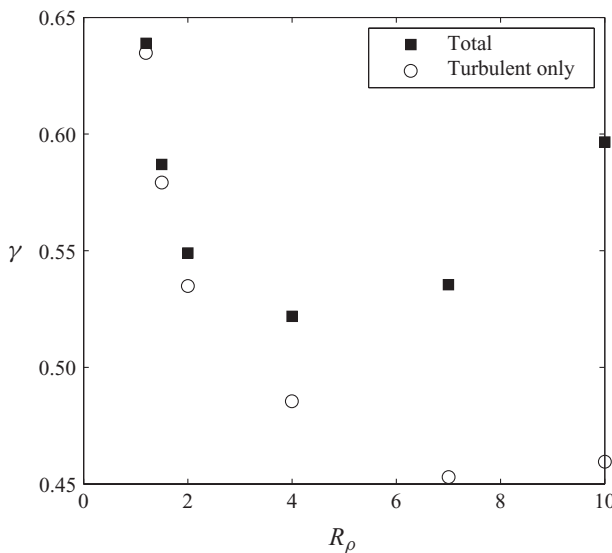

FIGURE 3. Comparison of the flux ratio γ^{tot} as calculated using the total heat and salt fluxes (both turbulent and convective) and γ as calculated using only the fluxes due to turbulent fingering convection. The diffusive contributions become important as R_ρ increases and the fingering fluxes drop, affecting not only the values of the flux ratio but also the location of the minimum of the curve.

Finally, we find that the Stern number A, which controls the dynamics of the collective instability, exceeds unity for $R_\rho \lesssim 7$ in the three-dimensional case, while two-dimensional simulations considerably underestimate A and therefore underestimate the range of R_ρ for which the system may be unstable to these modes.

Further discussion of the implications of these simulations is deferred to § 5. For now, the above results provide the necessary data to apply the mean-field theory of § 2 to the oceanic parameter regime.

R_0	Nu_0	γ_0	A_1	A_2
7.0	5.48	0.45	0.16	−11.61
4.0	13.3	0.49	0.27	−25.7
1.5	73.2	0.58	0.56	−217.31

TABLE 2. Empirically derived parameters for growth rate prediction using the unified theory at high, midrange, and low values of background density R_0. A_1 and A_2 are estimated by using neighbouring values of the density ratio.

4. Dominant modes of instability as a function of background density ratio

The flux laws determined above enable us to estimate the growth rates for the various mean-field modes of instability discussed in §2. As seen in §2.2.3, up to four modes of instability exist, but it is not immediately clear which mode dominates in the various regions of parameter space. To answer this question in the oceanic context, we now examine the solutions of the growth rate equation (2.13) for different values of R_0, with the corresponding γ_0, Nu_0, A_1 and A_2 calculated from the turbulent fluxes measured in §3 and shown in table 2. We then find the largest growth rate for a given mode geometry (as determined by k and l), maximising $\mathrm{Re}(\lambda)$ over the three roots of the cubic. Figure 4 shows this maximum growth rate as a function of wavenumber for three representative values of the background density ratio: $R_0 = 7$, where the fingering instability is weak, $R_0 = 1.5$, where the density gradient is close to unstable and turbulent fluxes are large (see table 2), and an intermediate value of $R_0 = 4$. The plots show l on a logarithmic scale to capture the wide range of relevant horizontal lengths, from the small filaments of the fingering instability up through extensive lateral intrusions. The horizontal and vertical axes have been switched to reveal the characteristic 'flower' structure of the instability region.

Since the growth rate of the fingering instability is recovered from our mean-field theory when A_1, A_2, etc, are zero (as discussed in §2.2.3), an analogous feature appears here even though A_1, $A_2 \neq 0$. This 'fingering' mode appears as a 'bulb' on all plots, at the smallest horizontal scales (large l) and large vertical scales (low k). Note, however, that mean-field theory should not be applied to model such small-scale structures. In practice, the bulb merely serves to indicate the region of l space ($\log l \geqslant -1$) above which the theory is no longer applicable.

At high density ratio (figure 4a), in the absence of lateral gradients, only the fingering mode remains. The presence of a lateral gradient introduces two additional regions of instability, one oscillatory and one direct, both confined to large vertical and horizontal scales (i.e. small k, l). These appear as 'leaves' in the diagram. As expected, lateral gradients break the symmetry of the solutions, since the $k\phi$ terms in (2.13) distinguish between positive and negative k perturbations. The direct mode corresponds to a lateral intrusion which typically grows on a time scale of about 30 h, with a horizontal scale of the order of a kilometre and vertical scale of a few metres (i.e. with a slope of the order of ϕ).

For an intermediate density ratio ($R_0 = 4$, figure 4b), the gravity waves of the collective instability appear at a range of vertical and horizontal scales starting at $l = 0.055$, $k = 0.06$ (a physical size of about a metre in each direction), with a growth time scale of about 30 h. The lateral gradient strongly modifies the gravity waves, increasing both their maximum growth rate and the size of the instability region for
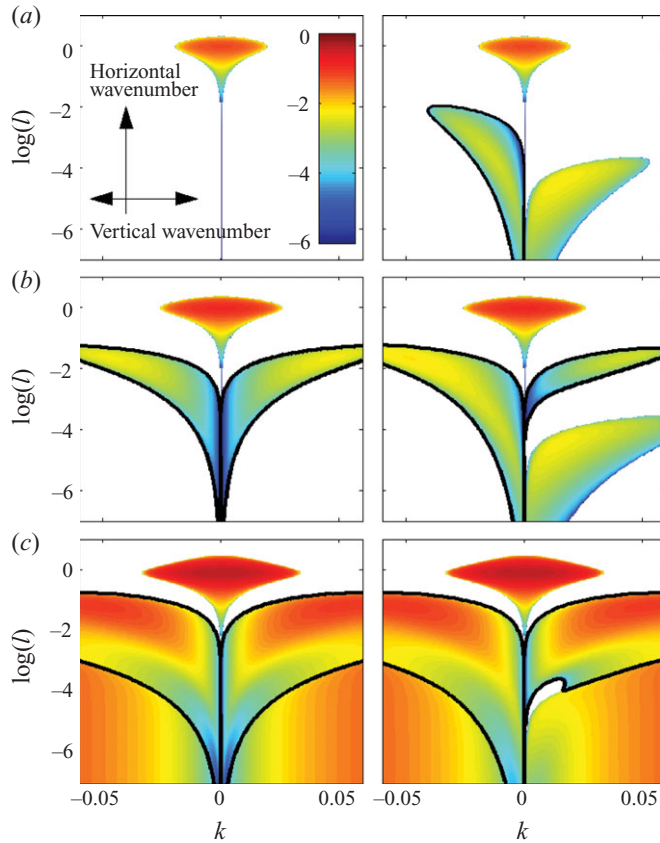
FIGURE 4. Predicted real part of growth rates for the fastest growing perturbations, where colour is scaled to $\log \text{Re}(\lambda)$. Only positive values are shown; the region is left white if no modes grow. The horizontal axis shows vertical wavenumber, and the vertical axis shows the logarithm of horizontal wavenumber to capture the broad range of expected scales. This particular display choice yields these characteristic 'flower plots'. The left-hand column shows results in the absence of lateral gradients ($\phi = 0$), while the right-hand column shows results for a typical oceanic value of $\phi = 0.01$. In each of the six figures, regions surrounded by a dark contour show oscillatory behaviour, by contrast with the direct modes. For example, the symmetric 'bulbs' at high l are direct modes, corresponding to the growth rate of individual fingers. (a) High density ratio ($R_0 = 7$). (b) Midrange density ratio ($R_0 = 4$). (c) Low density ratio ($R_0 = 1.5$).

negative k values, while suppressing growth for positive k. As with $R_0 = 7$, the lateral gradient also triggers a direct intrusive mode at large horizontal scales.

Finally, at low density ratios the system is dominated by the collective instability (oscillatory) and the γ- (direct) instability and is now unstable to a continuous range of modes on both large and small horizontal and vertical scales. At the scales for which the mean-field theory is valid ($k \ll 1$), the collective instability grows fastest, most unstable on scales of a metre both horizontally and vertically, and with a growth time scale around 2 h regardless of the presence of a lateral gradient ($\phi = 0.01$). For comparison, a γ-mode of the same vertical scale grows at roughly one third of this rate.

Figure 5 shows the growth rate of various modes in our theory at low density ratio ($R_\rho = 1.5$) and in the presence of lateral gradients ($\phi = 0.01$). Also shown are
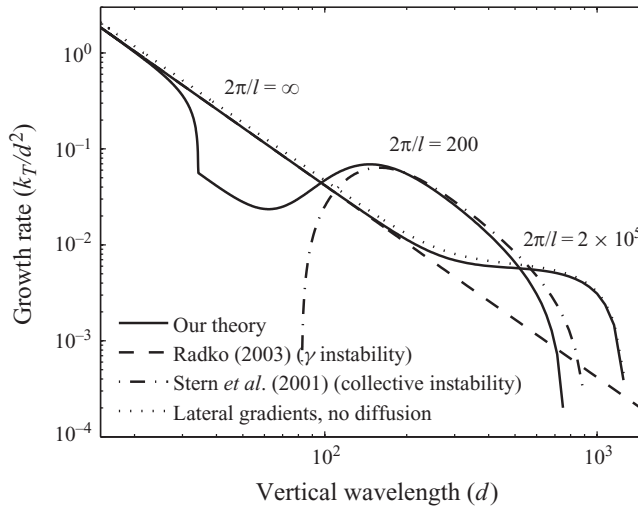
FIGURE 5. Comparison of the real component of projected growth rates between theories at $Pr = 7$, $\tau = 1/100$, for $R_0 = 1.5$ and $\phi = 0.01$. The $l = 0$ ($2\pi/l = \infty$) mode growth rate is identical to the one predicted by the γ-instability of Radko (2003); the remaining lines have horizontal perturbation wavelengths of $200d = 1.8$ m and $200\,000d = 1.8$ km. The mean-field theory captures both the collective instability at large vertical scales and the γ-instability at small vertical scales and matches well with the intrusive instability at the largest scales.

the growth rates of the collective instability of Stern *et al.* (2001), of the γ-instability of Radko (2003) and of the intrusive instability of Walsh & Ruddick (1995, ignoring Reynolds stresses). For a horizontally invariant perturbation ($l = 0$, equivalent to a domain width of $2\pi/l \rightarrow \infty$), the mean-field theory matches Radko's γ-instability. For perturbations with moderate horizontal scales ($2\pi/l = 200d$, approximately 2 m in dimensional terms), the unified theory predicts the presence of gravity waves with similar vertical scales and recovers the collective instability. As the vertical wavelength decreases, the mode inclination decreases, and it becomes a γ-mode. At the largest horizontal scales ($2\pi/l = 2 \times 10^5 d$, about 2 km), our theory recovers the growth rate of intrusive modes from Walsh & Ruddick (1995).

Using this unified formalism, we have therefore demonstrated how the dominant type of large-scale instability in salt-fingering systems depends strongly not only on the scale of the perturbations considered but also on the background density ratio. Field observations (You 2002) reveal that R_ρ can vary significantly in the ocean. In nearly convectively unstable regions ($R_\rho \rightarrow 1$), the collective and γ instabilities control the dynamics of the system (also see Part 2), but as the system becomes more stably stratified, these modes disappear and lateral gradients emerge as the dominant factor in the creation of large-scale structures.

5. Discussion and conclusions

5.1. *Turbulent flux laws*

The simulations of §3.2 are of direct relevance to the problem of parameterising double-diffusive mixing in the ocean. These problems arise in basin-scale ocean circulation models (Gargett & Holloway 1992; Zhang, Schmitt & Huang 1998;

Merryfield, Holloway & Gargett 1999) and in fine-scale studies focusing on the dynamics of intrusions, internal waves and thermohaline staircases (Walsh & Ruddick 2000; Stern & Simeonov 2002; Simeonov & Stern 2004; Radko 2005). While several attempts have already been made to deduce the small-domain flux laws from numerical simulations (Shen 1995; Stern *et al.* 2001; Stern & Simeonov 2005; Radko 2008), the computational restrictions in early studies precluded direct treatment of the oceanographic case (characterised by three-dimensional dynamics, $Pr = 7$, $\tau = 0.01$). Instead, simulations were either two-dimensional or employed diffusivity ratios significantly higher than the heat–salt value of 0.01. The double-diffusive flux laws were deduced by extrapolation of the numerical results obtained in the computationally accessible regime – an approach clearly requiring *a posteriori* validation. The simulations summarised in table 1 are the first DNS that meet the challenge of solving the actual heat–salt problem in three dimensions. A comparison of these results with earlier studies reveals a good qualitative agreement with earlier estimates. In retrospect, it is perhaps surprising to see how well the former educated guesses of flux laws (Schmitt 1981; Stern *et al.* 2001) captured the pattern of heat–salt diffusivities as a function of density ratio.

The comparison with oceanographic field measurements is more ambiguous since small-scale mixing in the ocean is driven by a combination of double diffusion and turbulence – their relative contribution is uncertain and much debated. Nevertheless, the careful analysis of the NATRE (North Atlantic Tracer Release Experiment) data set by St Laurent & Schmitt (1999) made it possible to evaluate the salt finger diffusivities directly from observations. The estimated salt diffusivity is characterised by a monotonically decreasing dependence on density ratio, reducing from $K_S = 50 \times 10^{-6} \, \text{m}^2 \, \text{s}^{-1}$ at $R_\rho = 1.4$ to $K_S = 10 \times 10^{-6} \, \text{m}^2 \, \text{s}^{-1}$ at $R_\rho = 1.8$ (St Laurent & Schmitt 1999). Once again, these values are in broad agreement with the DNS results summarised in table 1.

Finally, the presented synthetic data (table 1) make it possible to assess the relevance of several hypotheses proposed to explain the physics of equilibration. Most notably, Stern (1969) suggested that the amplitude of salt fingers could be limited by the collective instability, with equilibrium fluxes characterised by values of $A \sim 1$. A similar suggestion was put forward by Kunze (1987), who pointed out that Stern's (Stern 1969) criterion is equivalent to specifying the Richardson number based on scales of individual fingers and speculated that an increase in A above unity would be followed by the rapid destruction of fingers by secondary instabilities – an idea most recently revisited by Inoue *et al.* (2008). Our results, which reveal variations in A by 2 orders of magnitude, emphasise the limitations of Stern/Kunze hypothesis and motivate the search for alternative conceptual models.

5.2. *Large-scale instabilities and implications for the formation of thermohaline staircases*

In this paper, we have treated three proposed mechanisms for large-scale instability in salt-fingering systems, unifying under one framework what had previously been studied in isolation (Walsh & Ruddick 1995; Stern *et al.* 2001; Radko 2003). Note that a related approach to the problem, considering the effect of the Richardson number on the fluxes and focusing on thermohaline interleaving rather than the oscillatory modes of the collective instability, may be found in the recent work of Smyth & Ruddick (2010). In our work, as in theirs, considering all instability mechanisms in a single formalism opens the possibility of comparing the growth rates of the various mean-field modes to one another and establishing the dominant ones in each region

of parameter space. Furthermore, using the realistic flux laws discussed above, we are now able to give robust quantitative predictions for the presence and growth rates of each mode individually.

For the heat–salt system, we find that no single instability mechanism of those proposed is expected to dominate in all fingering-unstable regions of the ocean. At high density ratio ($R_\rho \geqslant 7$), for example, the Stern number drops below 1 and only lateral intrusions may be destabilised. As shown in §4, intrusive modes with horizontal scales on the order of a kilometre and vertical scales of a few metres are expected to grow on a time scale of about 30 h. As the density ratio decreases below seven, gravity-wave (collective instability) modes are also destabilised, growing fastest at horizontal and vertical scales of a few metres. The relative growth rates of the gravity waves and the intrusive modes depend sensitively on their spatial extent and on the slope of the isothermal contours (ϕ) with respect to the vertical, in a manner which can be evaluated through our theory. Finally, when the background stratification is close to neutral stability, which is the case for numerous fingering regions of the ocean, γ-modes are also unstable and grow on similar time scales as the gravity waves – on the order of a few hours, much faster than the intrusive modes.

These findings also enable us to place constraints on existing theories for the formation of thermohaline staircases. Indeed, all three mean-field modes of instability have been proposed to generate these structures in the process of their nonlinear development (Walsh & Ruddick 1995; Stern *et al.* 2001; Radko 2003). However, it is important to note that staircases are typically only observed to exist in very low density ratio environments ($R_\rho < 2$, see Schmitt 1981). We find that in this parameter regime (see figure 5), intrusions grow 1–2 orders of magnitude slower than gravity waves or γ-modes, unless lateral gradients are exceptionally strong (which could happen in some regions of the Mediterranean outflow, for example). This limits the relevance of intrusive modes when applied to the formation of staircases in the bulk of the thermocline. We also find that gravity-wave modes grow faster than γ-modes on all spatial scales for which mean-field theory is applicable (vertical wavelength greater than about $100d$, see the Appendix). This should *a priori* point to the collective instability as the mechanism responsible for the layer formation.

However, the aforementioned correspondence between the locations of observed oceanic staircases ($R_\rho < 2$) and interval of strongly decreasing $\gamma^{tot}(R_\rho)$ is too remarkable to be dismissed. In addition, the only existing numerical simulation to date for which staircase formation has been observed (Radko 2003) has unambiguously identified a γ-mode as the staircase precursor. For these reasons, the γ-instability could prove to be just as important as a generating mechanism for these large-scale structures. At this point, large-scale numerical simulations are the only avenue towards further progress, an avenue we follow in Part 2 of this paper.

Appendix. Numerical determination of flux laws

A.1. *Description of the numerical algorithm*

We measure the non-dimensional turbulent fluxes of heat and salt as functions of the density ratio using the following numerical algorithm. We solve the original set of equations (2.1a)–(2.1d) for homogeneous fingering convection using, as explained in §2.1, triply periodic boundary conditions for all perturbations, e.g.,

$$T(x, y, z, t) = T(x + L_x, y, z, t) = T(x, y + L_y, z, t) = T(x, y, z + L_z, t), \quad \text{(A 1)}$$

where (L_x, L_y, L_z) defines the dimensions of the computational box (in units of d). Note that in these units the global Rayleigh number of a simulation is equal to L_z^4. In this section, all quantities refer to the full field containing all scales (in contrast with §2.2).

We use a spectral algorithm based on the classical Patterson–Orzag method (Canuto *et al.* 2007) widely used for simulations of homogenous turbulence. Nonlinear products are evaluated on a grid in physical space, and the 3/2-rule is used to avoid aliasing errors (so N grid points in a coordinate direction correspond to Fourier modes up to wavenumbers of $N/3$ in that direction). Note that our simulation is a DNS, with no subgrid scale model. A third-order semi-implicit Adams-Bashforth/backward-differencing algorithm (Peyret 2002) is used for time stepping. All diffusive terms are treated implicitly, while the advection terms are explicitly treated. The above time-stepping method was chosen since it offers a relatively large stability domain that includes a part of the imaginary axis at a comparatively low cost. In order to guarantee numerical stability, the time step is adjusted dynamically. The code was designed to run efficiently on massively parallel supercomputers and employs a transpose-based parallel transform algorithm (Stellmach & Hansen 2008).

A.2. *Experimental protocol for determination of fluxes*

We are primarily interested in the high-Rayleigh number limit, where for fixed fluid parameters Pr and τ, the transport properties depend only on the background density ratio R_0. This implies the need to use a reasonably tall computational box ($L_z \gg 1$ in units of d). Our simulations must also permit a large-enough number of fingers to exist in the horizontal directions to provide good statistical estimates of the turbulent fluxes as well as avoiding artificial constraints on finger wavelength. On the other hand, the domain size should be small enough to suppress any secondary large-scale instabilities, which would drive the local density ratio R_ρ away from the background R_0 and modulate the turbulent fluxes we are trying to measure. After a careful study of the outcome of a series of simulations, further detailed below, we found that a computational domain of size $5 \times 5 \times 10$ in units of the FGW is a good compromise. The FGW is defined as the wavelength of the fastest growing mode of the fingering instability and depends on the model parameters Pr, τ and R_0 (see, e.g., figure 4 of Schmitt 1979).

After selecting a value of the density ratio, calculating the corresponding domain size in units of d and determining an appropriate spectral resolution for the simulations (see below, and table 1), we initialise the calculation with low-amplitude white noise perturbations in T and S, and let the system evolve with time. Vertical turbulent fluxes of heat and salt, defined as

$$\left.\begin{aligned} F_T &= \langle wT \rangle, \\ F_S &= \langle wS \rangle, \end{aligned}\right\} \quad \text{(A 2)}$$
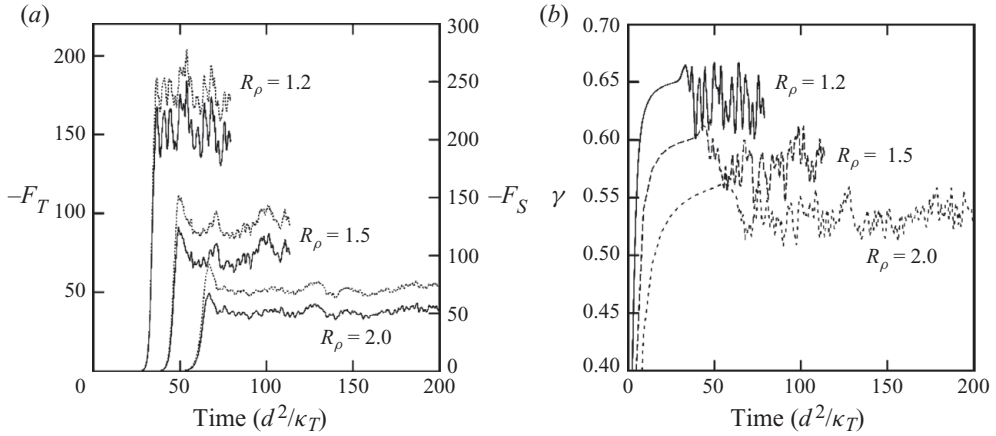
FIGURE 6. Time series derived from simulations of fingering convection in the heat–salt system ($Pr = 7$, $\tau = 0.01$) for the three cases $R_\rho = 1.2$, $R_\rho = 1.5$ and $R_\rho = 2.0$ (the first and third also shown in figure 1). (*a*) Fluxes $- F_T$ (solid line) and $- F_S$ (dotted line); note that for salt fingering F_T and F_S are both negative quantities, (*b*) Turbulent flux ratio γ.

are then computed, where $\langle \ldots \rangle$ denotes a volume average over the computational domain. Figure 6 shows time series of $- F_T$ and $- F_S$ (note that both fluxes are negative for fingering convection), as well as that of their ratio γ, for three values of R_ρ and for a fluid with the characteristic properties of salty water ($\tau = 0.01$, $Pr = 7$). After a period of exponential growth, the system settles into a statistically stationary finite amplitude state in which all plotted quantities fluctuate about well-defined temporal averages, the state of homogeneous fingering convection. The turbulent fluxes reported in table 1 are measured from temporal means of F_T and F_S once the system is in that state.

A.3. *The effect of the domain size*

In the last part of this appendix, we estimate the optimal box size for calculating local flux laws while meeting the criteria described above (large enough to provide good statistics, small enough to suppress secondary instabilities). Guidance for our choice can come from simulations in the less computationally demanding parameter regime of $Pr = 7$, $\tau = 1/3$. Empirically, we find that finger sizes are of the order 1 FGW horizontally and 5 FGW vertically, as shown in figure 7. These dimensions would suggest a computational domain of aspect ratio $1 : 1 : 5$, but to avoid possibly unnecessary computational expense, we first investigate whether a shorter box yields accurate results. Figure 8 shows the averaged Nusselt number and γ values for simulations from the two tested domains, one of approximately $5 \times 5 \times 8$ FGW (the 'small box') and the second approximately $6 \times 6 \times 20$ FGW ('medium box'). Comparison of the turbulent fluxes as a function of R_ρ along the fingering-unstable range $1 \leqslant R_\rho \leqslant 1/\tau$ shows strong agreement between the two sets of simulations except at the highest values of the density ratio, where some divergence occurs. Overall, these results suggest that the smallest box size provides sufficient statistics and a large-enough domain to yield accurate flux laws at most density ratios. In particular, the oceanic simulations discussed in §3 are conducted at $R_\rho \ll 1/\tau$, well away from the problematic behaviour that can be seen in figure 8 at high R_ρ. Meanwhile, neither set of simulations seem to exhibit any large-scale modes of instability, which also satisfies our requirements. This result is not surprising in the light of previous
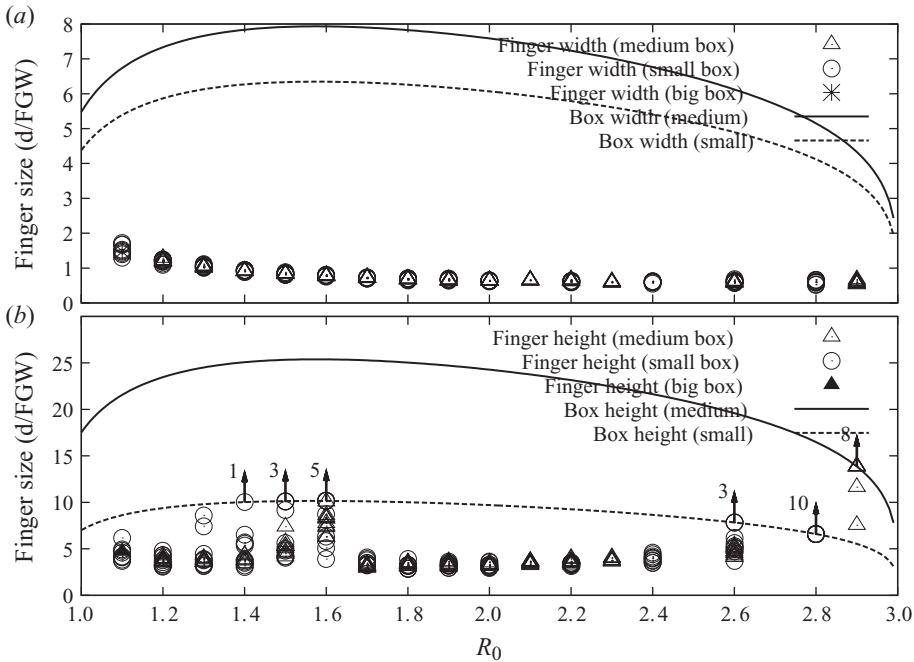
FIGURE 7. Numerically determined finger sizes for $Pr = 7$ and $\tau = 1/3$, sampling 10 points from each simulation over a range of density ratios at two box sizes: small box, $67d \times 67d \times 107.2d$, and medium box, $83.75d \times 83.75d \times 268d$. Estimates of finger height were taken using the autocorrelation of the vertical velocity, $f(s) = \int \int \int_V w(x, y, z)w(x, y, z + s)\,\mathrm{d}x\,\mathrm{d}y\,\mathrm{d}z$. We designate finger height as the distance s beyond which f drops below 0.05 (and similarly, using u, for the typical finger width). The single data point available from the large-domain simulation described in Part 2 is included for comparison. (*a*) Finger width demonstrating that both small and medium boxes are wide enough to contain many fingers in the horizontal dimension. In both boxes, finger widths are uniformly of the order of 1 FGW. (*b*) Finger height showing the effect of decreasing box size. Points located on the box height line represent sample times at which vertical velocity autocorrelation does not drop below the threshold value (i.e. fingers are taller than the box size); the corresponding numeric labels indicate the number of sampled points that exceeded the box height. In the small box overshoot occurs in two regions, $R_0 = 1.4$–1.6 and $R_0 \geqslant 2.6$. In the medium box, fingers only reach the box height for $R_0 \geqslant 2.9$.

three-dimensional simulations in very small domains (e.g. Stern *et al.* 2001), in which large-scale modes were also not observed. (For more detail on suppression of large-scale instabilities, see the analysis of the large-domain simulation in Part 2 of this paper.)

The difference between the turbulent fluxes measured in the two geometries at large density ratio can be understood in terms of a secondary instability, which is thought to cause the saturation of the fingers (Shen 1995). At the highest R_0 values, the unstable modes for the secondary instability are excluded by the smaller box, and finger velocities must reach much higher amplitudes before they are finally disrupted. Figure 9, which compares $Nu(t)$ in the two runs at $R_0 = 2.6$, shows the sharp artificial increase in fluxes that results in the shorter domain. Examination of the measured finger sizes at the same density ratio further demonstrates the effect (see figure 7). Fingers in the taller domain have heights of 4.1–5.3 FGW, while those in the shorter box (7.8 FGW high) are generally taller and exceed their domain height at several
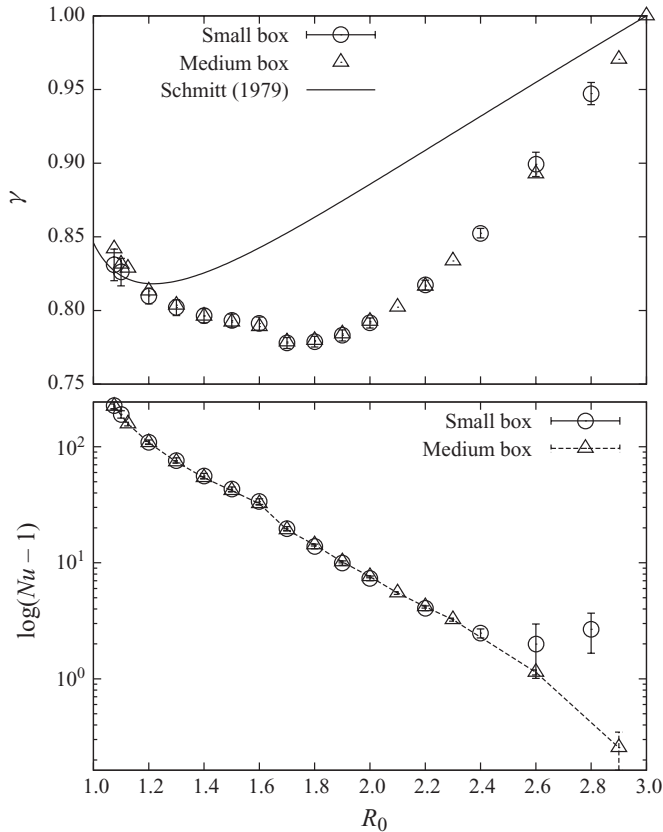
FIGURE 8. Small ($67d \times 67d \times 107.2d$) and medium ($83.75d \times 83.75d \times 268d$) box average values of the turbulent flux ratio $\gamma(R_0)$ and the logarithm of the Nusselt number $Nu(R_0)$. For most R_0 values the calculated small-box averages of Nu and γ closely compare with their medium-box counterparts, even where the finger height exceeds the small box height (identifiable in the bottom panel of figure 7). At large R_0, however, the averages diverge, seen in the logarithmic $(Nu_0 - 1)$ values.

of the sampled times. Thus, even though the true finger size (as observed in the larger box) should fit within the smaller domain, delaying the onset of the secondary instability artificially lengthens finger structure and inflates the fluxes.

For the purpose of extending mean-field theory to more difficult parameter ranges (such as $Pr \ll 1$, $\tau \ll 1$ of interest in the astrophysical context), these results provide a valuable guide. For most values of R_0, boxes of not more than $5 \times 5 \times 10$ FGW in height may be expected to provide robust flux averages while suppressing large-scale structures such as gravity waves that would otherwise swamp the finger field and complicate the averaging process. However, as the background density ratio increases towards a completely stable stratification, taller boxes are necessary to prevent artificial increase in the measured fluxes. In this regime it is particularly useful to examine the Nusselt number time series (or some other flux measure), where the signature of a too-small domain can be immediately recognized as in figure 9.

One final feature bears comment, namely the sharp increase and sudden decrease in finger height variability as R_0 increases above 1.6. This transition, apparently not a function of box size, corresponds to a kink in the $\gamma(R_\rho)$ curve (see figure 8), but speculation as to its cause is deferred to future work.
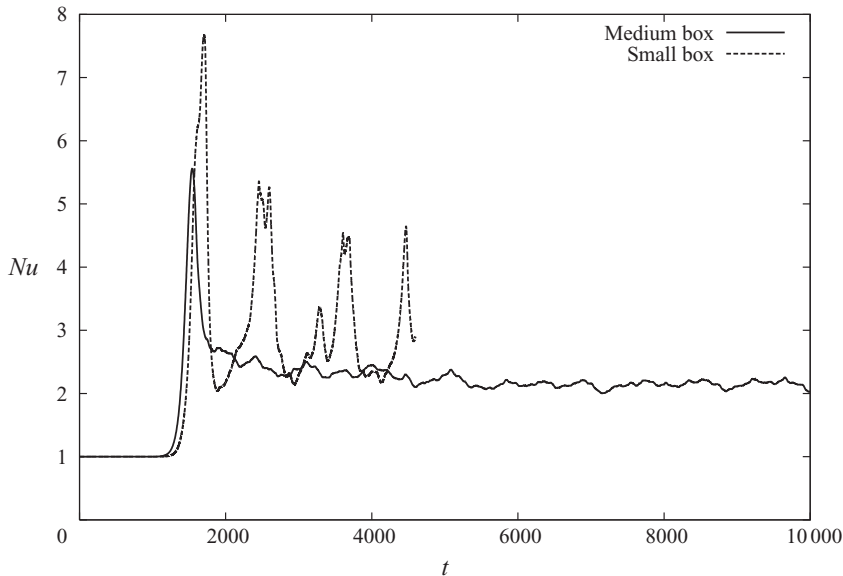
FIGURE 9. Nusselt number time series for the medium and small boxes at $R_0 = 2.6$, where fingers overshoot the small box height but are still contained in the medium box height (see figure 7). In the medium box, the Nusselt number quickly reaches a stable average with only small fluctuations, where the small box series varies widely.

REFERENCES

BAINES, P. G. & GILL, A. E. 1969 On thermohaline convection with linear gradients. *J. Fluid Mech.* **37**, 289–306.

BORUE, V. & ORSZAG, S. A. 1996 Turbulent convection with constant temperature gradient. In *APS, Division of Fluid Dynamics Meeting*, 24–26 November 1996, abstract no. CG.01. pp. 1.

CALZAVARINI, E., DOERING, C. R., GIBBON, J. D., LOHSE, D., TANABE, A. & TOSCHI, F. 2006 Exponentially growing solutions in homogeneous Rayleigh-Bénard convection. *Phys. Rev.* E **73** (3), 035301–035304.

CANUTO, C. G., HUSSAINI, M. Y., QUARTERONI, A. M. & ZANG, T. A. 2007 *Spectral Methods: Evolution to Complex Geometries and Applications to Fluid Dynamics*. Springer.

CHARBONNEL, C. & ZAHN, J. P. 2007 Thermohaline mixing: a physical mechanism governing the photospheric composition of low-mass giants. *Astron. Astrophys.* **467** (1), L-15–L-18.

DIETZE, H., OSCHLIES, A. & KÄHLER, P. 2004 Internal-wave-induced and double-diffusive nutrient fluxes to the nutrient-consuming surface layer in the oligotrophic subtropical North Atlantic. *Ocean Dyn.* **54** (1), 1–7.

GARAUD, P. 2011 What happened to the other Mohicans? The case for a primordial origin to the planet-metallicity connection. *Astrophys. J. Lett.* **728** (2), L30.

GARGETT, A. E. & HOLLOWAY, G. 1992 Sensitivity of the gfdl ocean model to different diffusivities for heat and salt. *J. Phys. Oceanogr.* **22** (10), 1158–1177.

GLESSMER, M. S., OSCHLIES, A. & YOOL, A. 2008 Simulated impact of double-diffusive mixing on physical and biogeochemical upper-ocean properties. *J. Geophys. Res.* **113**, C08029.

HOLYER, J. Y. 1981 On the collective instability of salt fingers. *J. Fluid Mech.* **110**, 195–207.

INOUE, R., KUNZE, E., ST. LAURENT, L., SCHMITT, R. W. & TOOLE, J. M. 2008 Evaluating salt-fingering theories. *J. Mar. Res.* **66**, 413–440.

KLUIKOV, Y. Y. U. & KARLIN, L. N. 1995 A model of the ocean thermocline stepwise stratification caused by double diffusion. In *Double-Diffusive Convection, Geophysical Monograph*, vol. 94, pp. 287–292. American Geophysical Union.

KRISHNAMURTI, R. 2003 Double-diffusive transport in laboratory thermohaline staircases. *J. Fluid Mech.* **483**, 287–314.

KUNZE, E. 1987 Limits on growing, finite-length salt fingers: a richardson number constraint. *J. Mar. Res.* **45**, 533–556.

KUNZE, E. 2003 A review of oceanic salt-fingering theory. *Prog. Oceanogr.* **56** (3–4), 399–417.

McDOUGALL, T. J. 1985a Double-diffusive interleaving. Part I. Linear stability analysis. *J. Phys. Oceanogr.* **15** (11), 1532–1541.

McDOUGALL, T. J. 1985b Double-diffusive interleaving. Part II. Finite amplitude, steady state interleaving. *J. Phys. Oceanogr.* **15** (11), 1542–1556.

MERRYFIELD, W. J., HOLLOWAY, G. & GARGETT, A. E. 1999 A global ocean model with double-diffusive mixing. *J. Phys. Oceanogr.* **29** (6), 1124–1142.

PEYRET, R. 2002 *Spectral Methods for Incompressible Viscous Flow*. Springer.

RADKO, T. 2003 A mechanism for layer formation in a double-diffusive fluid. *J. Fluid Mech.* **497**, 365–380.

RADKO, T. 2005 What determines the thickness of layers in a thermohaline staircase? *J. Fluid Mech.* **523**, 79–98.

RADKO, T. 2008 The double-diffusive modon. *J. Fluid Mech.* **609**, 59–85.

RUDDICK, B. & KERR, O. 2003 Oceanic thermohaline intrusions: theory. *Prog. Oceanogr.* **56** (3–4), 483–497.

RUDDICK, B. & RICHARDS, K. 2003 Oceanic thermohaline intrusions: observations. *Prog. Oceanogr.* **56** (3–4), 499–527.

RUDDICK, B. R. & TURNER, J. S. 1979 The vertical length scale of double-diffusive intrusions. *Deep Sea Res. Part* A. *Oceanogr. Res. Papers* **26** (8), 903–904, IN1–IN3, 905–913.

RUDDICK, B. R., PHILLIPS, O. M. & TURNER, J. S. 1999 A laboratory and quantitative model of finite-amplitude thermohaline intrusions. *Dyn. Atmos. Oceans* **30** (2-4), 71–99.

SCHMITT, R. W. 1979 The growth rate of super-critical salt fingers. *Deep-Sea Res.* **26A**, 23–40.

SCHMITT, R. W. 1981 Form of the temperature-salinity relationship in the central water: evidence for double-diffusive mixing. *J. Phys. Oceanogr.* **11** (7), 1015–1026.

SCHMITT, R. W. 1983 The characteristics of salt fingers in a variety of fluid systems, including stellar interiors, liquid metals, oceans, and magmas. *Phys. Fluids* **26**, 2373.

SCHMITT, R. W. 1994 Double diffusion in oceanography. *Annu. Rev. Fluid Mech.* **26** (1), 255–285.

SCHMITT, R. W., LEDWELL, J. R., MONTGOMERY, E. T., POLZIN, K. L. & TOOLE, J. M. 2005 Enhanced diapycnal mixing by salt fingers in the thermocline of the tropical atlantic. *Science* **308** (5722), 685.

SHEN, C. Y. 1995 Equilibrium salt-fingering convection. *Physics of Fluids* **7** (4), 706–717.

SIMEONOV, J. & STERN, M. 2004 Double-diffusive intrusions on a finite-width thermohaline front. *J. Phys. Oceanogr.* **34** (7), 1723–1740.

SIMEONOV, J. & STERN, M. E. 2007 Equilibration of two-dimensional double-diffusive intrusions. *J. Phys. Oceanogr.* **37** (3), 625–643.

SMYTH, W. D. & RUDDICK, B. 2010 Effects of ambient turbulence on interleaving at a baroclinic front. *J. Phys. Oceanogr.* **40** (4), 685–712.

ST. LAURENT, L. & SCHMITT, R. W. 1999 The contribution of salt fingers to vertical mixing in the north atlantic tracer release experiment. *J. Phys. Oceanogr.* **29** (7), 1404–1424.

STANCLIFFE, R. J., GLEBBEEK, E., IZZARD, R. G. & POLS, O. R. 2007 Carbon-enhanced metal-poor stars and thermohaline mixing. *Astron. Astrophys.* **464**, L57–L60.

STELLMACH, S. & HANSEN, U. 2008 An efficient spectral method for the simulation of dynamos in Cartesian geometry and its implementation on massively parallel computers. *Geochem. Geophys. Geosyst.* **9** (5), Q05003.

STELLMACH, S., TRAXLER, A., GARAUD, P., BRUMMELL, N. & RADKO, T. 2011 Dynamics of fingering convection. Part 2. The formation of thermohaline staircases. *J. Fluid Mech.* doi:10.1017/jfm.2011.99.

STERN, M. E. 1960 The 'salt fountain' and thermohaline convection. *Tellus* **12** (2), 172–175.

STERN, M. E. 1969 Collective instability of salt fingers. *J. Fluid Mech.* **35**, 209–218.

STERN, M. E. & SIMEONOV, J. A. 2002 Internal wave overturns produced by salt fingers. *J. Phys. Oceanogr.* **32** (12), 3638–3656.

STERN, M. E. & SIMEONOV, J. 2005 The secondary instability of salt fingers. *J. Fluid Mech.* **533** (−1), 361–380.

STERN, M. E. & TURNER, J. S. 1969 Salt fingers and convecting layers. *Deep-Sea Res.* **16** (1), 97–511.

STERN, M. E., RADKO, T. & SIMEONOV, J. 2001 Salt fingers in an unbounded thermocline. *J. Mar. Res.* **59** (3), 355–390.

TAIT, R. I. & HOWE, M. R. 1968 Some observations of thermohaline stratification in the deep ocean. *Deep-Sea Res.* **15**, 275–280.

TAIT, R. I. & HOWE, M. R. 1971 Thermohaline staircase. *Nature* **231** (5299), 178–179.

TOOLE, J. & GEORGI, D. 1981 On the dynamics of double diffusively driven intrusions. *Prog. Oceanogr.* **10**, 123–145.

TRAXLER, A., GARAUD, P. & STELLMACH, S. 2011 Numerically determined transport laws for fingering ('thermohaline') convection in astrophysics. *Astrophys. J. Lett.* **728** (2), L29.

VAUCLAIR, S. 2004 Metallic fingers and metallicity excess in exoplanets' host stars: the accretion hypothesis revisited. *Astrophys. J.* **605** (2), 874–879.

VERONIS, G. 2007 Updated estimate of double diffusive fluxes in the C-SALT region. *Deep-Sea Res. I* **54**, 831–833.

WALSH, D. & RUDDICK, B. 1995 Double-diffusive interleaving: the influence of nonconstant diffusivities. *J. Phys. Oceanogr.* **25** (3), 348–358.

WALSH, D. & RUDDICK, B. 2000 Double-diffusive interleaving in the presence of turbulence: the effect of a nonconstant flux ratio. *J. Phys. Oceanogr.* **30** (9), 2231–2245.

YOU, Y. 2002 A global ocean climatological atlas of the Turner angle: implications for double-diffusion and water-mass structure. *Deep-Sea Res.* **49** (11), 2075–2093.

ZHANG, J., SCHMITT, R. W. & HUANG, R. X. 1998 Sensitivity of the gfdl modular ocean model to parameterization of double-diffusive processes. *J. Phys. Oceanogr.* **28** (4), 589–605.